Nanoscale

PAPER

View Article Online
View Journal | View Issue

Cite this: *Nanoscale*, 2019, **11**, 22559

Metronidazole-functionalized iron oxide nanoparticles for molecular detection of hypoxic tissues†

Miriam Filippi, [a,b] Dinh-Vu Nguyen,[c] Francesca Garello, [d] Francis Perton,[c] Sylvie Bégin-Colin, [c] Delphine Felder-Flesch, [c] Laura Power[a,b] and Arnaud Scherberich *[a,b]

Being crucial under several pathological conditions, tumors, and tissue engineering, the MRI tracing of hypoxia within cells and tissues would be improved by the use of nanosystems allowing for direct recognition of low oxygenation and further treatment-oriented development. In the present study, we functionalized dendron-coated iron oxide nanoparticles (dendronized IONPs) with a bioreductive compound, a metronidazole-based ligand, to specifically detect the hypoxic tissues. Spherical IONPs with an average size of 10 nm were obtained and then decorated with the new metronidazole-conjugated dendron. The resulting nanoparticles (metro-NPs) displayed negligible effects on cell viability, proliferation, and metabolism, in both monolayer and 3D cell culture models, and a good colloidal stability in bio-mimicking media, as shown by DLS. Overtime quantitative monitoring of the IONP cell content revealed an enhanced intracellular retention of metro-NPs under anoxic conditions, confirmed by the *in vitro* MRI of cell pellets where a stronger negative contrast generation was observed in hypoxic primary stem cells and tumor cells after labeling with metro-NPs. Overall, these results suggest desirable properties in terms of interactions with the biological environment and capability of selective accumulation into the hypoxic tissue, and indicate that metro-NPs have considerable potential for the development of new nano-platforms especially in the field of anoxia-related diseases and tissue engineered models.

Received 1st October 2019,
Accepted 30th October 2019

DOI: 10.1039/c9nr08436c

rsc.li/nanoscale

1. Introduction

Nanotechnology developments have produced innovative tools that have had a tremendous impact on the field of biomedicine, attracting growing scientific interest especially for disease diagnosis and development of nano-based therapeutic strategies.[1–3] So far, a number of engineered nano-objects have been proposed for multifunctional purposes such as imaging platforms, biosensors, and photothermal, antimicrobial or chemotherapeutic agents.[4,5] Nanoparticles endowed with magnetic properties (MNPs) owe their success to their unique properties of biocompatibility, stability, and magnetic behavior, which make them perfect for interacting with biological systems with the possibility of remote control.[6,7] Iron oxide nanoparticles (IONPs) represent the most outstanding class of MNPs, exhibiting a crystalline structure based on Fe_3O_4 (magnetite) or γ-Fe_2O_3 (maghemite) and characterized by different scales and various tridimensional geometries.[8] On reducing their size, the IONPs acquire superparamagnetic properties that enhance their performance as contrast agents in magnetic resonance imaging (MRI), therapeutic agents for hyperthermia, drug delivery platforms, and tools for cell separation and detection.[9,10] In order to maximize the stability and solubility of nanoformulations in the biological milieu and their compatibility in a physiological environment, various types of molecular coatings have been developed. Even though thus far, the most common choices have been polymers, such as dextran, chitosan, polyethylene glycol (PEG) or polyvinyl pyrrolidone (PVP),[11] and the need for systematic approaches to simplify the synthesis of the molecular coating components and to optimize the specific physico-chemical characteristics of the outer shell (*e.g.* mechanical resistance, thickness, chemical groups exposed on the outer surface) has driven the search for new synthetic coating molecules. In this regard, dendrimers

[a]*Department of Biomedical Engineering, University of Basel, Gewerbestrasse 14, 4123, Allschwil, Basel, Switzerland. E-mail: arnaud.scherberich@usb.ch*
[b]*Department of Biomedicine, University Hospital Basel, University of Basel, Hebelstrasse 20, 4031 Basel, Switzerland*
[c]*Université de Strasbourg, CNRS, Institut de Physique et Chimie des Matériaux de Strasbourg, UMR 7504, F-67000 Strasbourg, France*
[d]*Molecular and Preclinical Imaging Centers, Department of Molecular Biotechnology and Health Sciences, University of Torino, Torino, Italy*
†Electronic supplementary information (ESI) available. See DOI: 10.1039/c9nr08436c

have attracted special interest due to the tunability of their properties and their modular synthetic generation.[12] Particularly, the direct grafting of small-sized and well defined dendrons on the surface of nanoparticles has proved to be a successful strategy for designing functional IONPs.[13] The dendrons can be strongly anchored to the IONP surface *via* biphosphonate tweezers, resulting in nanosuspensions with good colloidal stability in water and isoosmolar media.[14] Efficient dendrons based on oligoethyleneglycol units, one hexa or octaethyleneglycol chain ending with a carboxylate function, optionally adjoining two tetraethyleneglycol chains have already been synthesized in both linear and dendrimeric forms.[15]

Several kinds of IONPs have been conjugated with drugs, proteins, enzymes, antibodies, or nucleotides for delivery to target organs, tissues, or tumors. One of the most conventional applications is the hyperthermic treatment and molecular imaging of cancer cells.[16] Limited vascularization in solid tumors allows cancer cells to grow and survive, thus outcompeting normal cells in the microenvironment.[17] Decreased tissue oxygen tension is a component also found in many other intractable diseases, as well as an obstacle in several therapeutic approaches. For instance, the cell viability inside tridimensional tissue-like constructs for regenerative medicine is strongly dependent on the oxygenation level, since the diffusion of oxygen and nutrients to cells from capillary networks does not exceed 100–200 μm.[18] Because the low pressure of oxygen represents a marked feature of pathological tissues, the conjugation of bioreductive compounds to molecular probes has been extensively exploited to detect and reach hypoxic cells.[19] Bioreductive molecules are selectively reduced in hypoxic tissues, generating reactive intermediates that bind to intracellular molecules. For instance, nitroimidazole and its derivatives successfully deliver systems to poorly-perfused hypoxic regions in solid tumors.[19,20] The 5-nitroimidazole, metronidazole, becomes reductively activated by the pyruvate : ferredoxin oxidereductase system under anoxic conditions.[21] The anaerobic environment triggers metronidazole's capability to bind DNA and other intracellular macromolecules, enabling the stable accumulation of the drug inside the cells.[22–24] This property can be exploited to either selectively image hypoxic cells or to kill target cells (for instance for antimicrobial purposes).[25,26] Metronidazole has become a common starting material for the preparation of radiopharmaceuticals that efficiently recognize hypoxic tumors *in vitro* and *in vivo*, thanks to the ease of conjugation that preserves the specific sites of recognition and the biological activity of the ligand.[20] However, the use of non-radioactive IONPs as contrast agents would be preferable to avoid the limitations associated with radioactive tracers and to provide a nanosized platform for further treatment-oriented development (*e.g.*, as drug carriers, or hyperthermic agents). Hence, a system combining bioreductive compounds and IONPs would allow achieving an active recognition of the hypoxic gradients and their visualization in high space resolution by safe and versatile imaging based on the magnetic resonance.

In the present paper, a novel dendron functionalized with one unit of metronidazole (metro-dendron) was used to decorate the surface of spherical IONPs and create novel hypoxia-activated nanoparticles (metro-NPs). To make the NPs also optically traceable, the molecule was also further labeled with a fluorophore (Alexafluor647), as previously reported.[14] Here, we provide a preliminary *in vitro* characterization of the novel nanoparticles, investigate their interaction with the biological environment in terms of cytotoxicity, cell internalization and stability in fluids mimicking physiological conditions, and assess their capability of intracellular accumulation into the hypoxic environment.

2. Materials and methods

Synthesis of metronidazole-functionalized dendrons

The synthesis of dendrons was based on a previously reported protocol.[27] All the steps of the synthetic procedure are described in the ESI (Schemes S1–S4†), and the resulting products were characterized by ^{1}H and ^{31}P NMR spectroscopy (Fig. S2–S8†) with a NMR instrument equipped with ^{1}H (500 MHz), ^{13}C (125 MHz) and ^{31}P (121 MHz) probes (Bruker, Billerica, Massachusetts, USA). A benzyloxy-protected bisphosphonate (reported as intermediate **4** in Scheme S1†) was the key platform for diversification by functionalizing the phenolic group with a metronidazole moiety. The final deprotection of phosphonate groups was secured by heating to reflux a solution of metronidazole-bisphosphonate (namely, dendron **5** in Scheme S1†) in dichloromethane with trimethylsilylbromide.

Synthesis and functionalization of nanoparticles

In a 100 mL two-necked flask, iron(II) stearate (2.2 mmol, 1.38 g), oleic acid (4.4 mmol, 1.24 g) and dioctylether (20 mL) were mixed together. The resulting solution was heated up to 120 °C and kept for 1 h under magnetic stirring without a reflux condenser. Then, the magnetic stirrer was removed and the condenser was connected to the flask. The solution was heated up to 298 °C for 2 h with a heating rate of 5 °C min^{-1}. After cooling down, a black suspension was precipitated by the addition of acetone and collected. Finally, the NPs were washed three times with a 1 : 4 mixture of chloroform : acetone. To functionalize the NP surface, a nanoparticle suspension in THF (5 mg of iron) was mixed with compound **6** (Scheme S1,† 5.25 mg) in a 30 mL vial, which was further completed with 25 mL of THF. The mixture was magnetically stirred for 30 min, and then compound **7** (1.75 mg) was added to the reaction mixture, and stirred for 24 h. The resulting particles were centrifuged by the addition of cyclohexane, dispersed in water and washed by ultrafiltration through cellulose membranes with a nominal molecular weight limit (NMWL) of 3 kDa. Briefly, after introducing 25 ml of the water suspension in the apparatus, the purification occurred by pressurizing the solution flow: whereas solvent and ungrafted molecules went through the membrane, the grafted NPs did not pass through and were redispersed in 25 ml of water and then subjected to

another ultrafiltration step. This was done five times.[13] The metro-NPs were obtained by coating the bare IONPs with metro-dendrons **6** and unfunctionalized dendrons **7** at a ratio of 3 : 1. This ratio was obtained by stoichiometrically adding metro-dendrons and unfunctionalized dendrons to the iron oxide suspension, before characterizing through infrared spectroscopy (Fig. S11†). Being the molecular area of a dendron governed by the surface area of the three-branched oligoethylene glycol (OEG) chains, it was possible to estimate by theoretical calculation that the number of dendrons grafted at the 10 nm-sized IONP surface could be around 600.[28] NPs decorated at 100% by the unfunctionalized dendrons were used as controls.[28] To make the NPs also optically traceable, the dendrons were also further labeled with a fluorophore (Alexafluor647), as previously reported.[14]

TEM

For the morphological studies, transmission electron microscopy (TEM) images of the IONPs in the organic medium were recorded with a JEOL 2100 TEM instrument (JEOL, Tokyo, Japan), operating at 200 kV, with a point-to-point resolution of 0.5 nm.

Dynamic light scattering

Dynamic light scattering (DLS, Zetasizer Nano 90 ZS, Malvern, UK) allowed for the determination of the mean hydrodynamic diameter of vesicles and their polydispersity index (PDI). In order to calculate the particle size, a scattering angle of 90 degrees was used. All measurements were performed in triplicate at 25 °C. Zeta potential measurements were initiated immediately after purification by ultrafiltration of the samples and carried out in triple samples, measured three times each at 21 °C and pH 5.3.

Cell lines

All cell lines were obtained from the American Type Culture Collection (ATCC, Manassas, VA, USA) and were tested for mycoplasma (MycoAlertTM Mycoplasma Detection Kit, Lonza AG, Basel, Switzerland). Murine macrophages (RAW 264.7 cell line) were cultured in monolayer at 37 °C in a 5% CO_2-containing humidified atmosphere in Dulbecco's modified Eagle's medium (DMEM). The medium was supplemented with 10% (v/v) heat-inactivated fetal bovine serum (FBS), 2 mM glutamine, 100 U mL^{-1} penicillin, and 100 μg mL^{-1} streptomycin (all from ThermoFischer Scientific, Switzerland). Human umbilical vein endothelial cells (HUVEC) were cultured in M199 medium supplemented with 20% FBS, 100 mg mL^{-1} endothelial cell growth supplement, 50 IU mL^{-1} heparin, 100 IU mL^{-1} penicillin, and 100 mg mL^{-1} streptomycin.

Cell viability tests

In the perspective of their potential use for biomedical applications, the biocompatibility of the dendronized nanoparticles underwent a series of cytotoxicity tests in order to evaluate their compatibility with living systems. HUVEC cells were incubated with the nanoparticles in the culture medium at different concentrations (ranging from 5 to 150 μg mL^{-1}) and for various time ranges (from 1 h to 2 days) at 37 °C. Then, the cell viability was estimated *via* the trypan blue exclusion assay. The reported viability percentages represent the average ratios between the number of viable cells, N_v, and the total number of cells, N_{tot} ($N_v/N_{tot} \times 100$). Moreover, cytotoxicity results were further studied by assessing the release of the cytoplasmic enzyme, lactate dehydrogenase (LDH), into the media from damaged or dead cells with leaky membranes.[29,30] For the LDH cytotoxicity assay, the cells were seeded in 24 well-plates at a concentration of 2.0×10^4 cells per well. After 12 h, a 100 μL aliquot of the media was collected and the released LDH was quantified by mixing with an NADH-buffered solution and pyruvate solution. The LDH activity was measured spectrophotometrically by following the conversion of NADH to NAD^+, at 340 nm.[29] The results are expressed as a percentage of the respective controls, representing the basal LDH released by cells incubated with the culture medium in the absence of NPs. Additionally, cell viability was assessed by the mitochondria-dependent reduction of MTT to formazan. After labeling, 2.0×10^4 cells per well were seeded in 48-well plates. After 24 h, the cells were incubated with 1 mL per well of MTT (0.5 mg mL^{-1}) at 37 °C. Approximately 4 to 6 h were required to produce formazan; supernatants were discarded and formazan was then dissolved in DMSO. The solutions were transferred to a 96-well plate and the extent of MTT reduction to formazan within the cells was quantified by the measurement of the optical density at 550 nm. The results are expressed as a percentage of the respective control (incubation in medium in the absence of NPs). Duplicate measurements were performed in three independent experiments.

Proliferation rate assessment

The proliferation rates of endothelial cells (HUVEC) and macrophages (RAW 264.7) after a 3 h incubation with nanoparticles at two different dosages (25 and 75 μg mL^{-1}) were monitored over 8 days. Briefly, 2.5×10^4 cells per well were seeded in 24-well plates and their proliferation rate was assessed with the CyQuant direct cell proliferation assay according to the manufacturer's protocol. The optical density (OD) was measured at 535 nm (530 to 560 nm excitation) in order to determine the amount of DNA in the wells 6 and 12 h and 1, 2, 4, and 8 days after incubation. The corresponding cell numbers were found by using calibration curves obtained from the same batch of cells and plotted against the culture time to obtain the proliferation rate curves.

3D regenerative models with NP-labeled cells

Stromal vascular fraction (SVF) cells were isolated from adipose tissues.[31,32] Briefly, liposuctions were obtained from 15 healthy donors after informed consent and according to a protocol approved by the Ethical Committee of the Canton of Basel (Ethikkommission beider Basel [EKKB], Ref. 78/07). The isolation of SVF cells was carried out by enzymatic digestion at 37 °C for 45 min with 0.075% collagenase type II (Worthington Biochemical Corp., Lakewood, NJ) and centrifugation

(1700 rpm, 10 min), as previously described.[33] Finally, a complete medium (CM) consisting of α-MEM supplemented with 10% fetal bovine serum (FBS), 1% HEPES, 1% sodium pyruvate, 1% penicillin (10 000 U mL^{-1}), streptomycin (10 000 μg mL^{-1}) and L-glutamine (29.2 mg mL^{-1}) solution (PSG solution, ThermoFisher Scientific, Switzerland) was used to suspend the cells before they were filtered through a 100 μm strainer (Sarstedt, Numbrecht, Germany) and counted. For NP labeling, the cells were incubated with a medium containing 25 μg mL^{-1} NPs for 3 h at 37 °C, washed with PBS three times, and directly used to generate the constructs. The 3D constructs were obtained from the co-assembly of SVF cells, fibrin, and fragments of decellularized matrix of adipose-derived scaffolding materials, as previously reported.[33] The final constructs (final volume of 40 μL) were maintained under standard culture conditions for 3 days before testing the proliferation rate and metabolic activity of seeded cells over time.

Proliferation and metabolic activity in 3D constructs

DNA quantification was performed with a commercially available fluorescence based kit (Quant-iTTM PicoGreen® dsDNA kit, #P7589, Invitrogen) according to the manufacturer's instructions following the mechanical disruption of constructs by pipetting and resuspension of the material into double distilled water. Fluorescence was measured with a Spectra Max Gemini XS microplate spectrofluorometer (Molecular Devices) with excitation and emission wavelengths of 485 nm and 538 nm, respectively. The alamarBlue assay was performed to determine the metabolic activity of seeded cells. The culture medium was supplemented with 10% (v/v) of alamarBlue reagent solution at 0.1 mg mL^{-1} (#R7017, Sigma-Aldrich) and incubation was carried out for 4 h at 37 °C before the fluorescence signal (at 570 and 600 nm) was measured with a Synergy H1 microplate reader (Biotek). Fluorescence intensity values were normalized to internal controls. The metabolic activity per cell was normalized to both the cell number and fluorescence intensity values of the first experimental time point (day 0).

Internalization and retention of nanoparticles by the cells

In order to assess the internalization rate of nanomaterials, the cells (HUVEC and Raw264.7, 1.0×10^6) were incubated with medium containing NPs (25 μg mL^{-1}, 37 °C) for various time ranges. Then the cells were washed with PBS three times, centrifuged, and re-suspended in 10% SDS. After 1 min of vortexing, the homogenates were heated at 70 °C, and the amount of NPs inside the cell suspensions was estimated by iron quantification based on spectrophotometric absorbance according to the following formula:

$$\mathrm{Fe}(\mu g\ mL^{-1}) = (A_{370\ nm} - (B \times A_{750\ nm}))/S_{370\ nm}$$

where the ratio $A_{370\ nm}/A_{750\ nm}$ represents lysed unlabeled control cells and $S_{370\ nm}$ represents the slope of the Fe standard curve. B is the correction factor for turbidity to convert absorbance from the cellular absorbance at 750 nm to its 370 nm equivalent so that through subtraction, only the iron is measured. Since the nanoparticles were decorated with the fluorophore Alexafluor647, the internalization was also assessed by counting the number of cells positive for fluorescence at 647 nm. The ratio between the positive cells and number of nuclei (DAPI positive) represented the positive fraction on the observed population. After incubation (37 °C, 3 h, 25 μg mL^{-1}), the retention of NPs inside HUVEC cells was assessed over time and quantified by fluorescence intensity. The optical density (emission at 650 nm) of NP-labeled cells was measured. Finally, the release of nanoparticles from 3D constructs containing SVF cells pre-labeled with NPs (37 °C, 3 h, 25 μg mL^{-1}) was also assessed by quantification of iron in the culture medium by measuring the absorbance at 370 nm. The inhibition of clathrin-mediated endocytosis was tested by co-incubation with 100 μM chlorpromazine (CPZ) hydrochloride (C8138, Sigma-Aldrich, Switzerland).

Stability in biological media

The stability of NPs in biological media was investigated by incubating them in cell culture medium (DMEM), with Human Serum Albumin (HSA) solution (0.65 mM, pH 7.4) or reconstituted Human Serum (HS) (50 mg mL^{-1}, pH 7.4) to simulate the plasmatic environment. Incubations with PBS and HEPES were used as controls. Appropriate amounts of HSA (Sigma-Aldrich, St Louis, USA) and freeze-dried aliquots of HS proteins (SERO, Billingstad, Norway) were reconstituted to obtain a final protein concentration in the incubation sample, mimicking physiological conditions. Incubation tubes were maintained at 37 °C. In order to test the occurrence and the possible effects of the interaction between proteins and NPs, the level of NP aggregation was studied through DLS, in terms of size and polydispersity changes. Since DLS measurements can be severely affected by the presence of proteins, the samples were previously dialyzed using membranes with a 100 kDa molecular weight cut-off, which permit the transit of proteins, but prevent the passage of the much bigger NPs.

Hemolysis assay

The haemocompatibility of metro-NPs was evaluated according to the *in vitro* red blood cell (RBC) hemolysis test. The white cells were first removed from human blood samples, obtained from Blutspendezentrum, at the University Hospital of Basel. Finally, erythrocytes were dissolved in PBS at 2% concentration and mixed with an equal volume of physiological saline, NPs, and metro-NPs of 0.5 mg ml^{-1}, respectively. A positive hemolysis control was prepared by adding an equal volume of erythrocyte suspension and distilled water. After the mixture was maintained for 1 and 3 h at 37 °C and then centrifuged at 2000 rpm for 5 min, the supernatants were detected with a microplate reader (Bio-Rad, Hercules, CA) at 570 nm. The percentage of hemolysis was calculated by the equation: hemolysis (%) = $(OD_t - OD_{nc})/(OD_{pc} - OD_{nc}) \times 100$, where OD_T, OD_{NC}, and OD_{PC} refer to the absorbance values of the sample, negative control, and positive control, respectively.

Histological staining

The constructs were fixed overnight in a 4% paraformaldehyde solution. If necessary, the samples were decalcified in a 7% EDTA solution, before being embedded into paraffin. Histological sections (4.5 μm thickness) were stained with hematoxylin and eosin (#GHS116 and #HT110116, respectively, from Sigma Aldrich).

Hypoxia induction

Hypoxic cells were obtained either by a long incubation under hypoxic conditions (1% O_2) or by chemical induction. Specifically, in the latter case, the cellular hypoxia was triggered by adding the chemical inducer of hypoxia-inducible factor, cobalt(II) chloride hexahydrate ($CoCl_2{\cdot}6H_2O$),[34] to the culture medium. A 25 mM stock solution of $CoCl_2$ in bidistilled water was prepared immediately before use and added to the cell culture medium for a final concentration of 100 μM.[35] The cultures were incubated for 24 h in a conventional incubator (37 °C, 5% CO_2). Also the hypoxic tissue constructs and pellets for MRI were obtained through $CoCl_2$-chemical induction.

Prussian blue staining of cells

After IONP internalization, the cells were washed twice with PBS and fixed with 4% paraformaldehyde solution for 30 min at room temperature. After washing again twice with PBS, the cells were incubated with the Prussian blue staining solution, namely a 1 : 1 mixture of 4% potassium ferrocyanide (Sigma-Aldrich) and 4% hydrochloric acid (Sigma-Aldrich) for 15 min at room temperature and finally, washed with distilled water three times. The counterstaining was done for cytoplasm with eosin (Panreac Química S.L.U) for 5 min at room temperature. After washing, the cells were observed using inverted light microscopy (Olympus IX83, Life Science, Germany). All experiments were carried out in triplicate.

In vitro magnetic resonance imaging of cell phantoms

The cells were seeded at a density of 2.0×10^6 in a 75 cm^2 tissue culture flask, labeled with nanoparticles as described before, washed with PBS three times and kept in culture under either hypoxic or normoxic conditions for 3 days. After detachment, the cells were fixed with 4% formalin for 30 min, washed twice with PBS, and counted. 1.0×10^6 cells were collected by centrifugation, suspended in 50 μl PBS and transferred to glass capillaries. The capillaries were centrifuged (5 minutes, 1500 rpm), and loaded onto a support for *in vitro* MRI containing an agar-based matrix to avoid susceptibility artifacts due to air. The capillaries were imaged on their axial section in a Bruker Avance 300 spectrometer (Billerica, Massachusetts, USA) equipped with a micro-imaging probe working at 7.1 T. $T_{1\ w}$-images were acquired using a standard $T_{1\ w}$-MSME (MultiSlice MultiEcho). The first set of images was acquired with a sequence set with the following parameters: Time of Repetition (TR) = 200 ms, Time of Echo (TE) = 3.74 ms, Field of View (FOV) = 1.2×1.2 cm^2, matrix size = 128×128 pu (pixel units), slice thickness = 1.0 mm, number of slices = 3, and average number = 16, for a final acquisition time (TA) of 6 min 49 s. A standard saturation recovery protocol was used to measure T_1 relaxation times: variable TR = 50, 100, 200, 400, 600, 1000, 1500, 3000, 5000, and 8000 ms, for a final acquisition time of 42 min 39 s. The $T_{2\ w}$-images were acquired using a $T_{2\ w}$-RARE (Rapid Acquisition with Refocused Echoes) sequence with (TR) = 4000 ms, FOV = 1.20×1.20 cm^2, slice thickness = 1 mm, number of slices = 3, average number = 8, RARE factor = 32, TE = 3.9 ms, effective TE = 58.70 ms, and matrix = 128×128 pu, for a final acquisition time (TA) of 2 min 8 s. A MSME protocol was used to measure T_2 relaxation times: variable TE = 14, 28, 42, 56, 70, 84, 98, 112, 126, 140, 154, 168, 182, 196, 210, 224, 238, 252, 266, and 280 ms, for a final acquisition time of 8 min 32 s. The percentage T_1 and T_2 Contrast Variation (T_2-CV) was calculated on the $T_{1\ \mathrm{weighted}}$ and $T_{2\ \mathrm{weighted}}$-images. The mean Signal Intensity (SI_0) was calculated on ROIs manually drawn on the cell pellets and then normalized with respect to the signal produced by the unlabelled cell pellets ($SI_{n\text{-unlabeled}}$), in order to obtain the normalized signal intensity of labeled cell pellets, $SI_{n\text{-label}}$. The T_2-CV was calculated with respect to the normalized signal measured for the cells incubated with neat PBS ($SI_{n\text{-ctrl}}$), by applying the following expression: $T_{1/2} - \mathrm{CV}\ [\%] = (SI_{n\text{-label}} - SI_{n\text{-unlabeled}})/SI_{n\text{-unlabeled}} \times 100$. The percentage relaxivity variations (R_1/R_2 V) were calculated by applying an equivalent formula with values of relaxivity (R_1 and R_2) extracted from MRI relaxivity measurements: $R_1/R_2\ \mathrm{V}\ [\%] = (R_{n\text{-label}} - R_{n\text{-unlabeled}})/R_{n\text{-unlabeled}} \times 100$.

Statistics

Statistical analysis was performed with OriginPro 8.5 (OriginLab, Northampton, MA, USA). All variables are expressed as mean ± SD. Data have been acquired from at least four independent experiments, unless otherwise stated. To assess statistically relevant differences between two experimental groups, the *t*-test was used ($P < 0.05$ and $P < 0.01$ are expressed as * and **, respectively). A general linear two-way ANOVA test was used to verify the hypothesis whether there were changes in various parameters over time among the experimental groups and to identify relevant variations among several experimental groups.

3. Results

Synthesis of metro-dendrons

The coating of NPs was generated through dendrons synthesized according to a previously reported procedure.[27] In this way, a benzyloxy-protected bisphosphonate (indicated as intermediate **4** in Scheme S1†) was prepared to be used as the initial platform for subsequent deprotection and functionalization on the phenolic group with a metronidazole-derivatized OEG chain, and for further preparation of the bisphosphonic acid. These three final steps provided a good overall yield (69%) without compromising the purity, finally producing the metro-dendron, namely compound **6** shown in Fig. 1A.

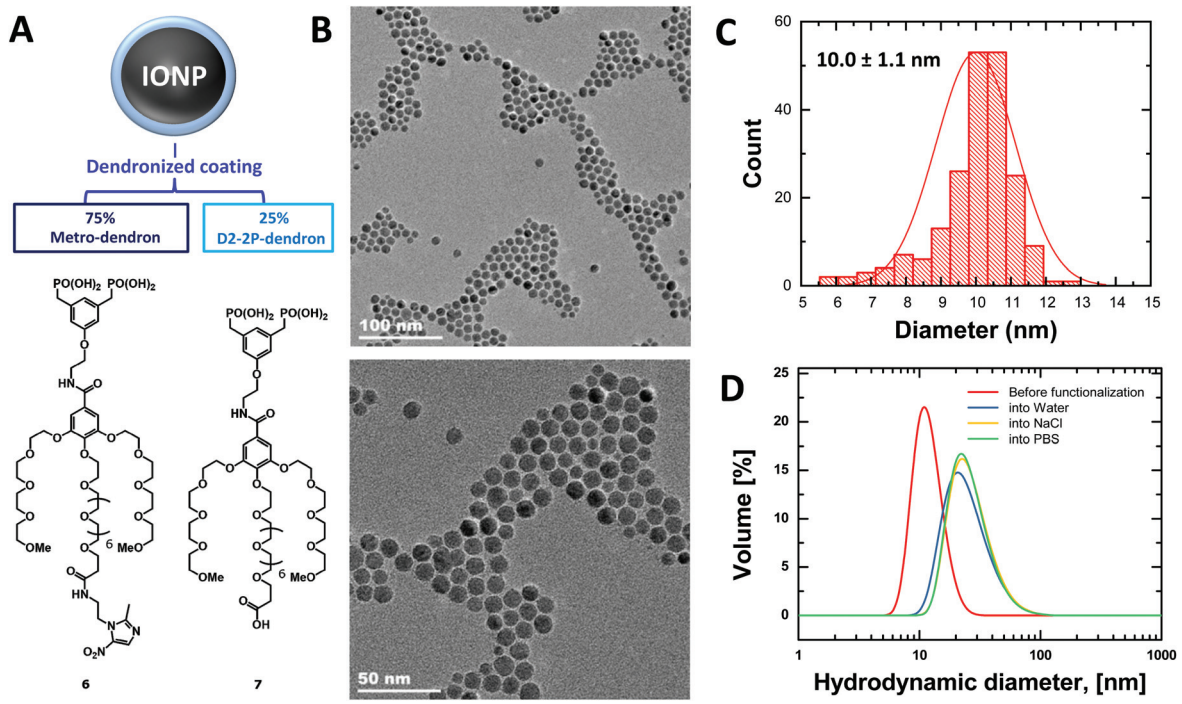

Fig. 1 Metro-functionalized dendronized nanoparticles. (A) Iron oxide nanoparticles (IONPs) were coated with a dendrimeric-based outer shell, composed of metronidazole-functionalized dendrons and unfunctionalized dendrons at a ratio of 3 : 1. Schemes of the first generation phosphonated dendrons grafted onto the IONP surface are provided (referred to as compounds **6** and **7**). (B) Transmission electron microscopy (TEM) images of dendronized nanoparticles in water suspension at increasing magnifications. (C) Particle size distribution of IONPs determined by dynamic light scattering (DLS). (D) DLS of IONPs before functionalization and of dendronized IONPs as water, saline buffer, and phosphate buffered saline (PBS) suspensions.

Characterization of nanoparticles and suspensions

The metro-NPs were obtained by coating the bare IONPs with metro-dendrons **6** and unfunctionalized dendrons **7** at a ratio of 3 : 1 (Fig. 1A). IONPs decorated by the unfunctionalized dendron only were used as controls (NPs).[28] The NP morphology and size were observed by TEM and DLS. A suspension of homogeneously sized particulate was obtained (Fig. 1B and S9–S11†), where the dendronized-coating increased the mean hydrodynamic diameter of NPs from their original size of 10 nm to around 20 nm (Fig. 1C and D). Moreover, the zeta-potential measured for metro-NPs slightly differed from that found for the unfunctionalized counterparts, corresponding to −6.4 ± 0.6 mV and −11.1 ± 0.7 mV, respectively.

Effects of metro-NPs on the viability and proliferation of cells grown in monolayer

For their prospective use in biomedical applications, the impact of the dendronized nanoparticles on cell viability was first assessed on human umbilical vein endothelial cells (HUVEC) grown in monolayer and exposed to different nanomaterial concentrations for various time durations. The nanoparticles displayed a high level of biocompatibility with short incubation times and low NP dosages; the viability was always above 80% (Fig. 2A, B and S12†), and even under the harshest conditions, namely the combination of the longest incubation time (two days) and the highest dosage (150 μg Fe mL^{-1}), the viability only dropped by 20%. The effects induced by the targeted nanoparticles (metro-NPs) did not substantially differ from those caused by the untargeted controls (NPs). Moreover, neither of the two formulations altered the proliferation ability of HUVECs and murine macrophages (RAW 264.7 cell line): after 3 h of incubation in the presence of intermediate NP dosages (25 and 75 μg Fe mL^{-1}), all cells showed growth trends comparable to the control cells incubated with equivalent volumes of PBS (Fig. 2C, D and S13†).

3D regenerative models with NP-labeled cells

In order to test the utility of NPs in biological applications, we labelled the cells employed to generate 3D *in vitro* tissue constructs. The stromal vascular fraction (SVF), a potent primary cell source easily isolated from adipose tissue, was used.[31,33,36] The cells were labelled with NPs (3 h, 25 μg Fe ml^{-1}) and co-assembled with fibrin and the AT-derived matrix (Fig. 3A). The constructs were kept in culture for 3 days before the proliferation rate and the metabolic ability of cells was tested *via* alamarBlue assay over time (Fig. 3B and C). After 3 weeks of culture, the SVF cells labeled with metro-NPs and NPs displayed similar metabolic and proliferation rates to the unlabeled controls.

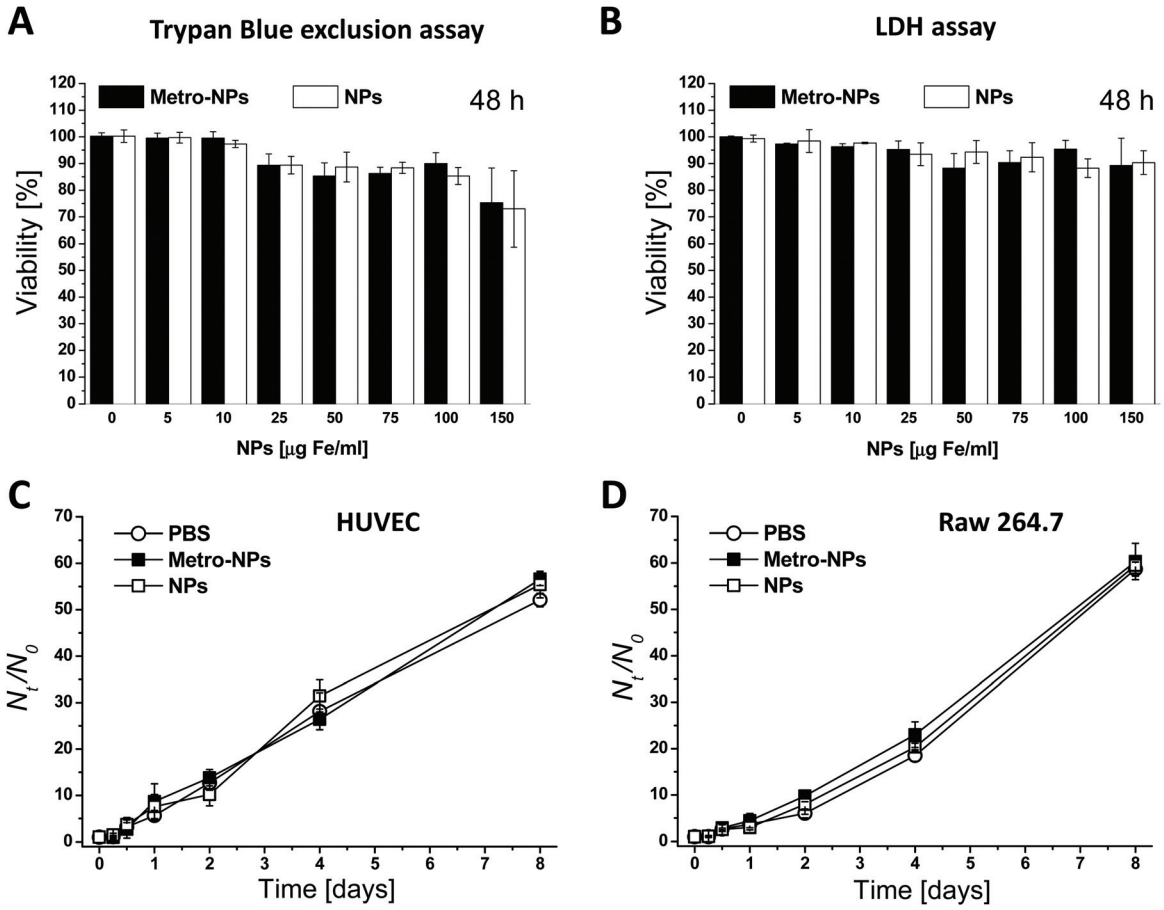

Fig. 2 Effects of retro-NPs on the viability and proliferation ability of cells grown in monolayer. Viability of HUVEC cells after incubation (37 °C) with different dosages of functionalized and unfunctionalized nanoparticles (metro-NPs and NPs), as tested by (A) trypan blue exclusion and (B) LDH cytotoxicity assays. Proliferation rates of (C) HUVECs and (D) Raw264.7 cells after incubation (37 °C, 3 h) with metro-NPs and untargeted NPs (25 μg Fe mL^{-1}). Equivalent volumes of PBS in the culture medium were used as controls.

Internalization and retention of NPs

As assessed by the spectrophotometric quantification of iron in the cell homogenates, the amount of nanoparticles internalized by the endothelial cells and macrophages after incubation at a fixed NP concentration (25 μg Fe mL^{-1}) increased with longer exposure times (Fig. 4A). After 6 h of incubation, 3.5/4.0 pg Fe per cell was measured, revealing a relatively fast internalization trend as compared to other nanoformulations and labeling procedures.[37,38] The functionalization of NPs with the metro-vector did not alter the internalization rate, as the two nanoformulations were taken up at similar rates. Similar conclusions were obtained by counting the fraction of fluorescence-positive cells after labeling with NPs additionally decorated with the fluorochrome Alexa647 (Fig. 4B and S14†). After labeling, the HUVECs retained the nanoparticles for around three days when grown in monolayer under standard culture conditions (Fig. 4C), whereas almost all NPs (≈90% of the initial iron amount) were found in the supernatants of 3D-constructs seeded with SVF cells at this time point (Fig. 4D). Furthermore, in order to determine the internalization mechanism of IONPs, the intracellular distribution was followed by histological observation after incubation in the presence or absence of chlorpromazine (CPZ), an inhibitor of clathrin-dependent endocytosis. Fig. 4E reproduces some representative images after Prussian blue staining experiments showing a high labeling efficiency under these conditions, with the NPs reaching almost 100% of the cells and distributed homogeneously in the intracellular space outside the nucleus. Moreover, in the presence of CPZ, the staining predominately marked the cell boundaries, possibly highlighting the adherence of the IONPs to the cell surface. However, the internalization was drastically reduced, thus suggesting that the uptake under regular labeling conditions mostly occurs through an endocytosis-dependent pathway.

Stability in biological media

The colloidal stability of NPs in biological media was investigated by incubating them in culture medium supplemented with human serum albumin (HSA) solution (0.65 mM) or reconstituted human serum (50% in volume) under conditions designed to simulate the plasmatic environment (0.65 mM, 37 °C, pH 7.4). The effects of interaction with proteins and par-

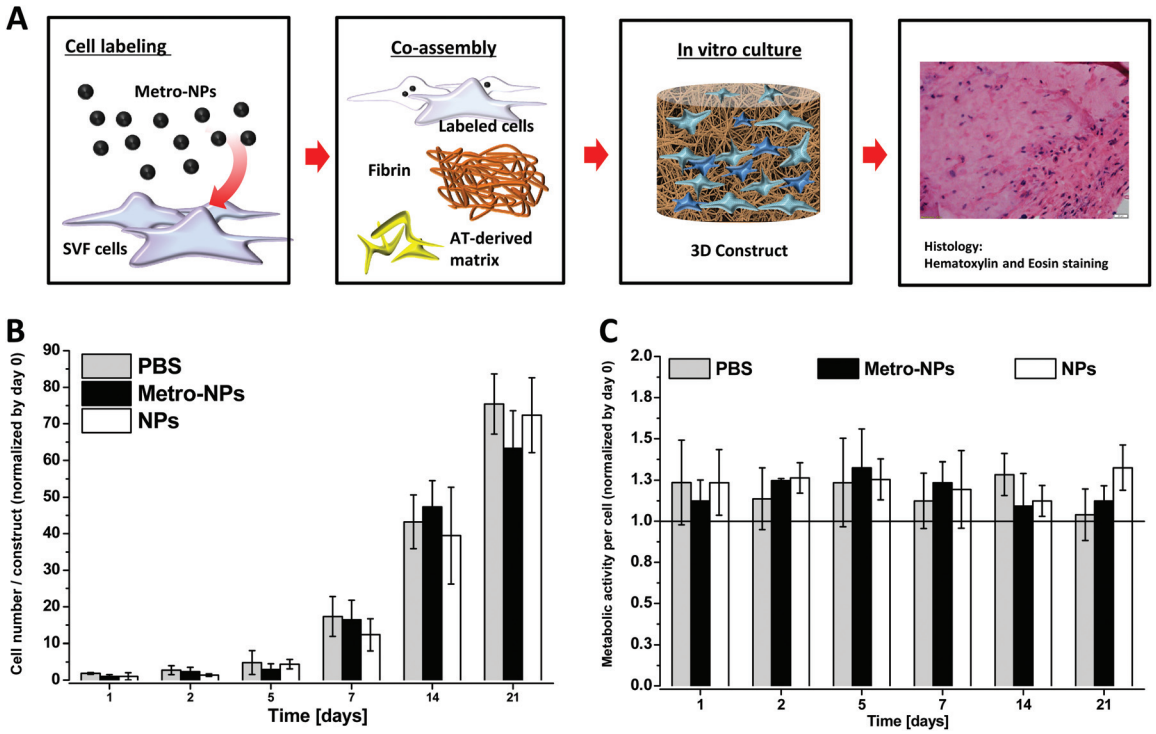

Fig. 3 Generation of 3D constructs and assessment of cell number and metabolism. (A) 3D constructs were obtained through the co-assembly of NP-labeled cells, fibrin, and adipose tissue-derived matrix (AT-derived matrix). The constructs were kept in culture for 3 days before the (B) viability and (C) metabolism were assessed with the alamarBlue assay on the supernatants.

ticle aggregation were monitored by DLS over time (Fig. 5). The polydispersity index (PDI) of NPs and metro-NPs in PBS or HEPES was always below 0.2, thus confirming prolonged stability in the buffer solution. No apparent aggregation occurred in the cell culture medium or in the HSA solution. In the presence of human plasma, the NP size was uniform during the first 24 h, although a small portion of aggregates was found at 48 h for both the formulations. However, this scattered size distribution only contained around 10% population with an average size of thousands of nanometers, but without massive precipitation. The metro-functionalization did not alter the capability of dendronized coating to prevent the formation of large aggregates under conditions mimicking a physiological environment, thus predicting a good stability in *in vitro* cell culture medium and *in vivo* blood circulation. Finally, as shown in Fig. 5F, over 3 h incubation in human blood no significant hemolysis of erythrocytes was induced by NPs and metro-NPs as compared to the normal saline group.

IONP retention in hypoxic cells

The capability of IONPs to specifically detect the hypoxic cells was assessed. Briefly, after culturing with a low tension of oxygen or exposure to chemical hypoxia-inducer $CoCl_2$, the cells were labeled with IONPs and their iron content was measured over time and compared to that of the cells grown under aerobic conditions. The rationale of this experimental procedure was based on the assumption that metronidazole exposed on the surface of IONPs might react with intracellular components in a reductive environment and then accumulate at a higher rate (Fig. 6A). The amount of initially internalized IONPs was comparable among all conditions, but 1 and 3 days after labeling, a higher amount of iron was quantified in hypoxic cells incubated with metro-NPs (Fig. 6B and C). A three-fold increased iron content was measured in the hypoxic cells incubated with metro-NPs (Fig. 6C) further confirmed by measuring the fluorescent signal at 647 nm (Fig. 6D) and histological inspection by Prussian blue staining (Fig. S15†). Finally, under hypoxic conditions, a different kinetics of iron release was also observed in 3D tissue constructs containing SVF cells pre-labeled with metro-NPs. In fact, in these constructs, the metro-NPs were retained for longer times as compared to the untargeted NPs (Fig. S16†), which instead were released with a trend comparable to that observed in constructs cultured under a normoxic atmosphere (Fig. 4D).

In vitro magnetic resonance imaging of cell pellets

Effective hypoxia-induced NP retention was also assessed by testing the MRI performance of the labeled cells *in vitro* (Fig. 7A) on human primary stem cells (ASCs, Fig. 7B) and a breast cancer cell line (MCF7, Fig. 7C). Three days after labeling with metro-NPs, the hypoxic pellets (Fig. 7B) of both ASCs and MCF7 appeared as the darkest ones on T_2-weighted images ($T_{2\ w}$-images), producing a decrease in the percentage T_2 contrast variation (T_2-CV) equivalent to ≈2.1 and 1.8 times

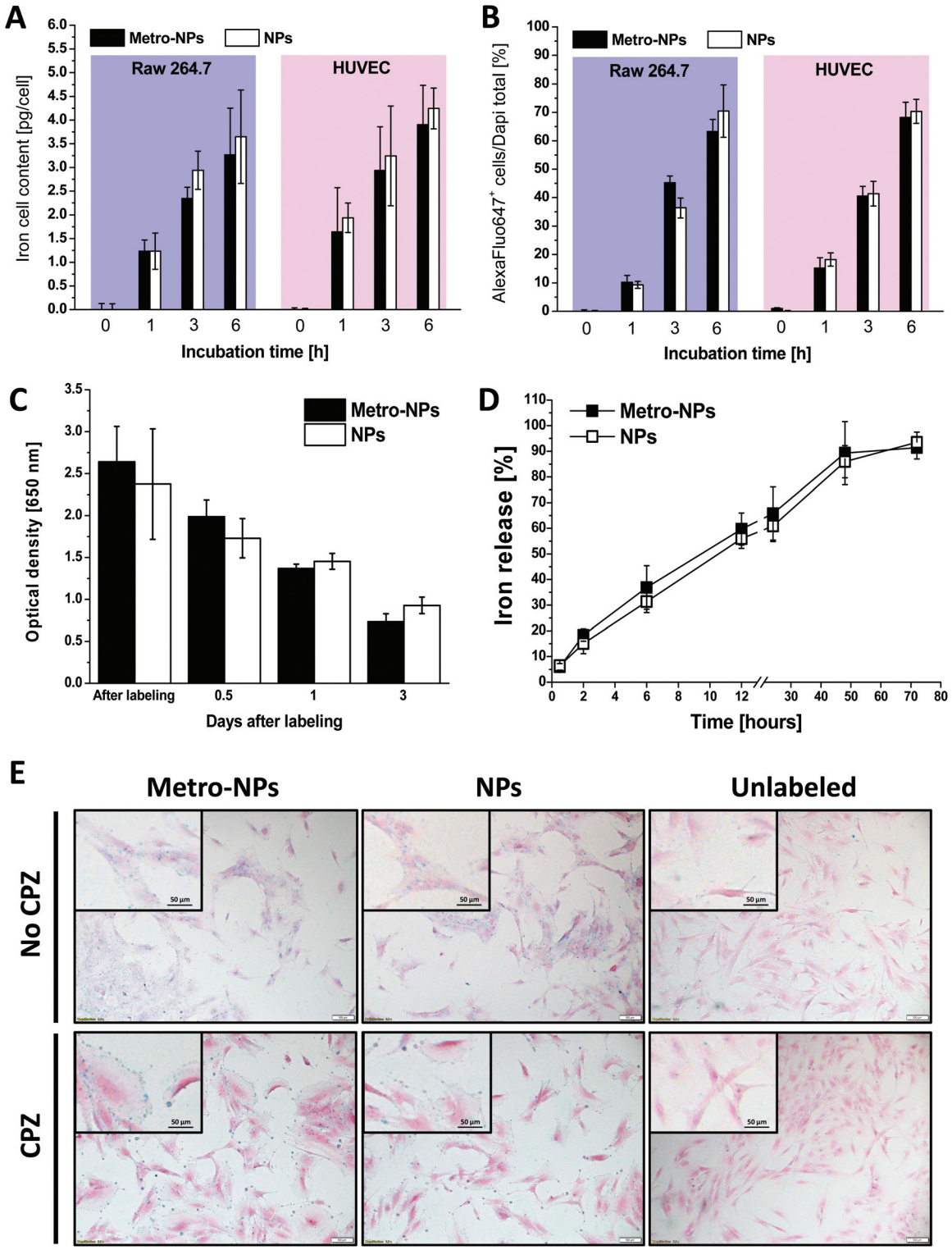

Fig. 4 Internalization and retention of NPs by cells. (A) Amount of iron quantified in the cells and (B) percentages of fluorescence-positive cells after incubation with fluorescently (Alexafluor647) labeled nanoparticles (metro-NPs and control NPs, 25 µg Fe mL^{-1}) for various time ranges. Retention of NPs inside HUVECs over time after incubation (37 °C, 3 h, 25 µg Fe mL^{-1}) as quantified by fluorescence intensity. (C) The optical density (emission at 650 nm) of the NP-labeled cells. (D) Release of nanoparticles from constructs containing SVF cells pre-labeled with NPs (37 °C, 3 h, 25 µg Fe mL^{-1}), iron in the culture medium was quantified by measuring the absorbance at 370 nm. (E) Internalization and retention of NPs, shown by Prussian blue staining of HUVEC cell cultures immediately after labeling under regular oxygen tension (top row). Equivalent volumes of PBS in the culture medium were used as controls (unlabeled). The addition of the endocytosis-inhibitor, CPZ, drastically reduced the uptake of IONPs (bottom row).

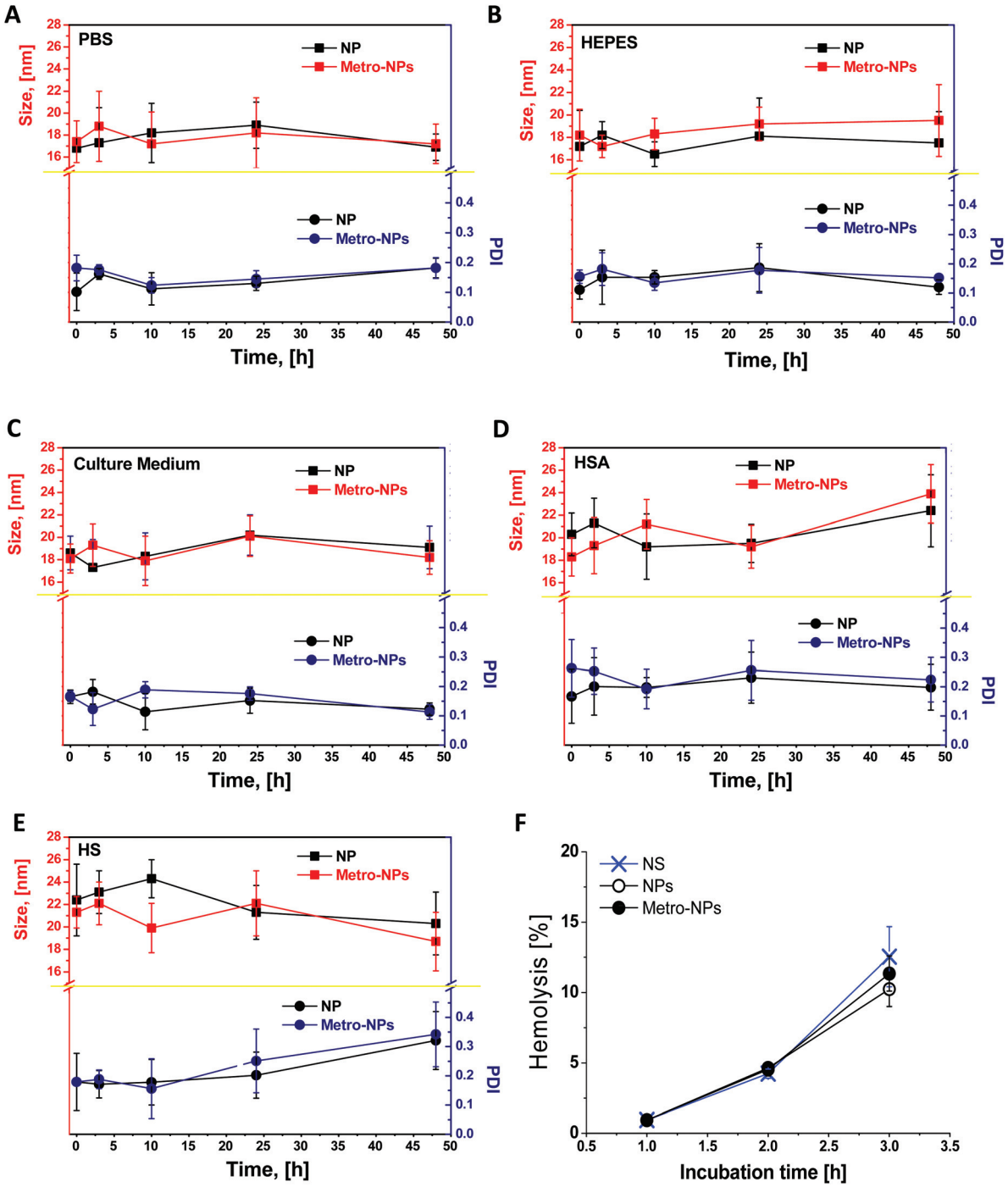

Fig. 5 Colloidal stability in biological fluids and hemolytic effects. Mean hydrodynamic diameter (size, nm) and polydispersity index (PDI) of functionalized and unfunctionalized nanoparticles (metro-NPs and control NPs) monitored by DLS over time, after incubation at 37 °C and pH 7.4 into buffered solutions and fluids mimicking the biological environment. Incubations were performed in (A) PBS, (B) HEPES buffer, (C) DMEM cell culture medium, (D) HSA solution, and (E) and reconstituted HS. Hemolysis ratio *in vitro* after NPs and metro-NPs (0.5 Fe mg ml^{-1}) treatment along different times (F).

the one induced by control NPs, respectively (Fig. S17†). Under normoxic conditions, the two labeled cell pellets showed comparable T_2-CV values resembling those of the NP-labeled hypoxic cells, thus highlighting no specific activity of the targeted system. Similar results were obtained in MCF7 cells (MCF7, Fig. 7C), thus suggesting the opportunity of efficient hypoxic tumor imaging. Water relaxation rates in the cell pellets were also measured in order to calculate the percentage relaxivity variations (R_1 and R_2 V) induced by the nanosystems under different conditions, finding good accordance with the

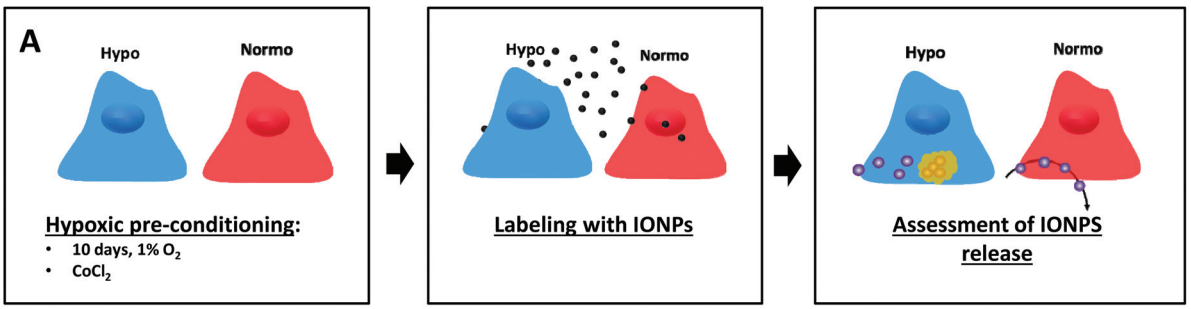

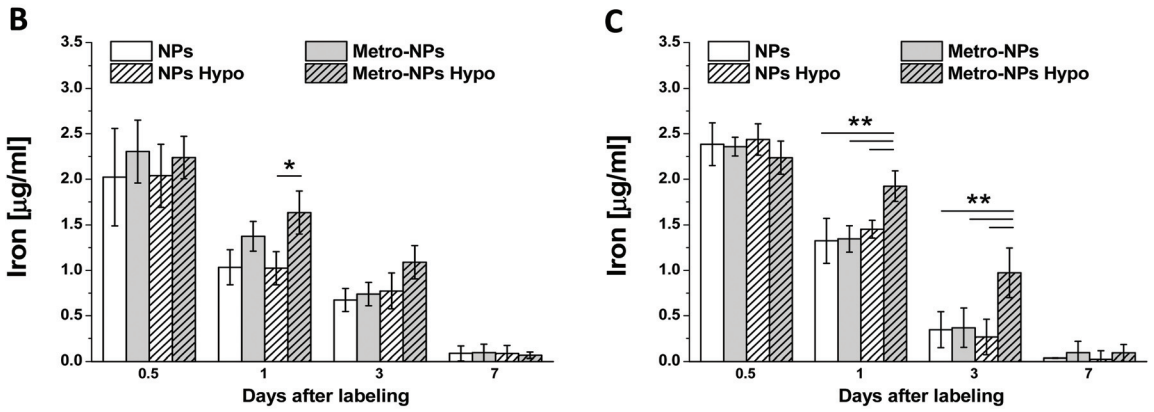

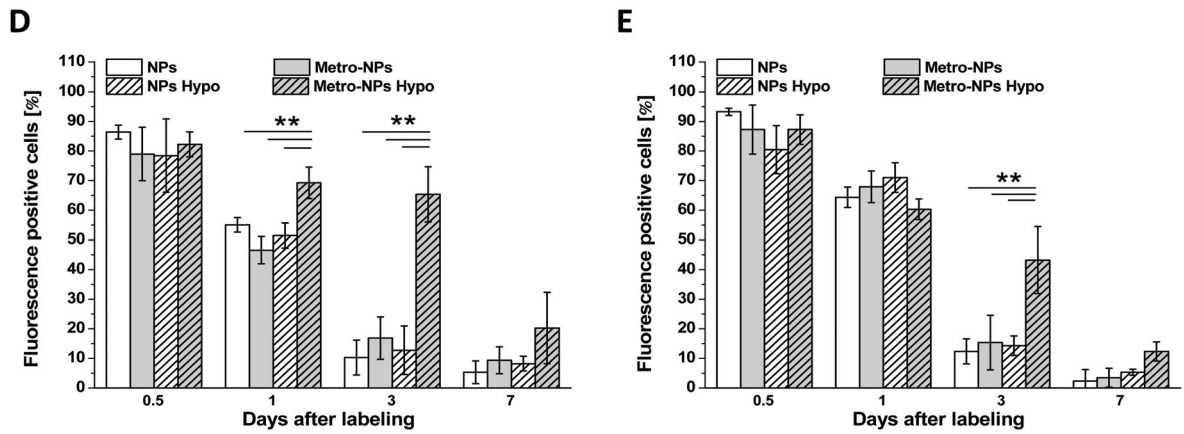

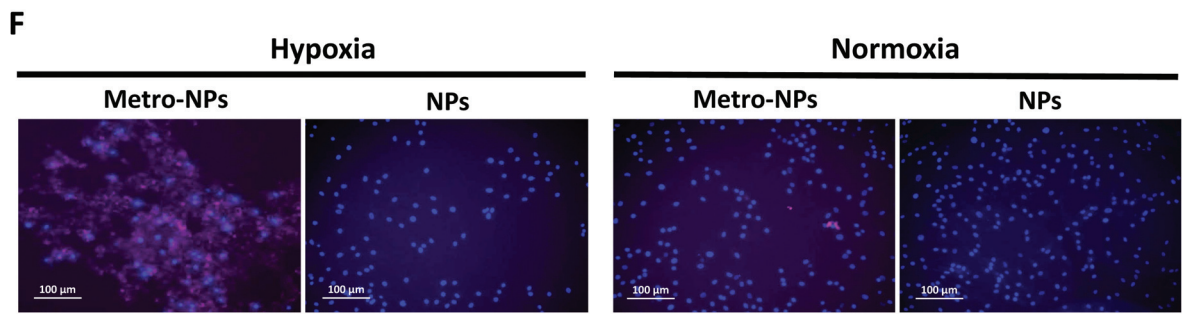

Fig. 6 Retention of IONPs in hypoxic cells. Scheme of the experimental procedure for the assessment of IONP retention after labeling of hypoxic cells. (A) Hypoxic cells were obtained either by a long incubation under hypoxic conditions (1% O_2) or by exposure to a chemical inducer of hypoxia-inducible factor, $CoCl_2$. IONP retention in the cell cultures after exposure to hypoxic conditions, obtained by incubation in (B and D) low O_2 pressure or (C and E) in the presence of $CoCl_2$. The iron content of cell suspensions was assessed at several time points over 1 week after the initial labeling by quantifying (B and C) cell iron content or (D and E) fluorescence intensity at 647 nm. (F) Representative fluorescence microscopy images of cell cultures 3 days after exposure to $CoCl_2$-induced hypoxic conditions (hypoxia) or control standard incubation (normoxia).

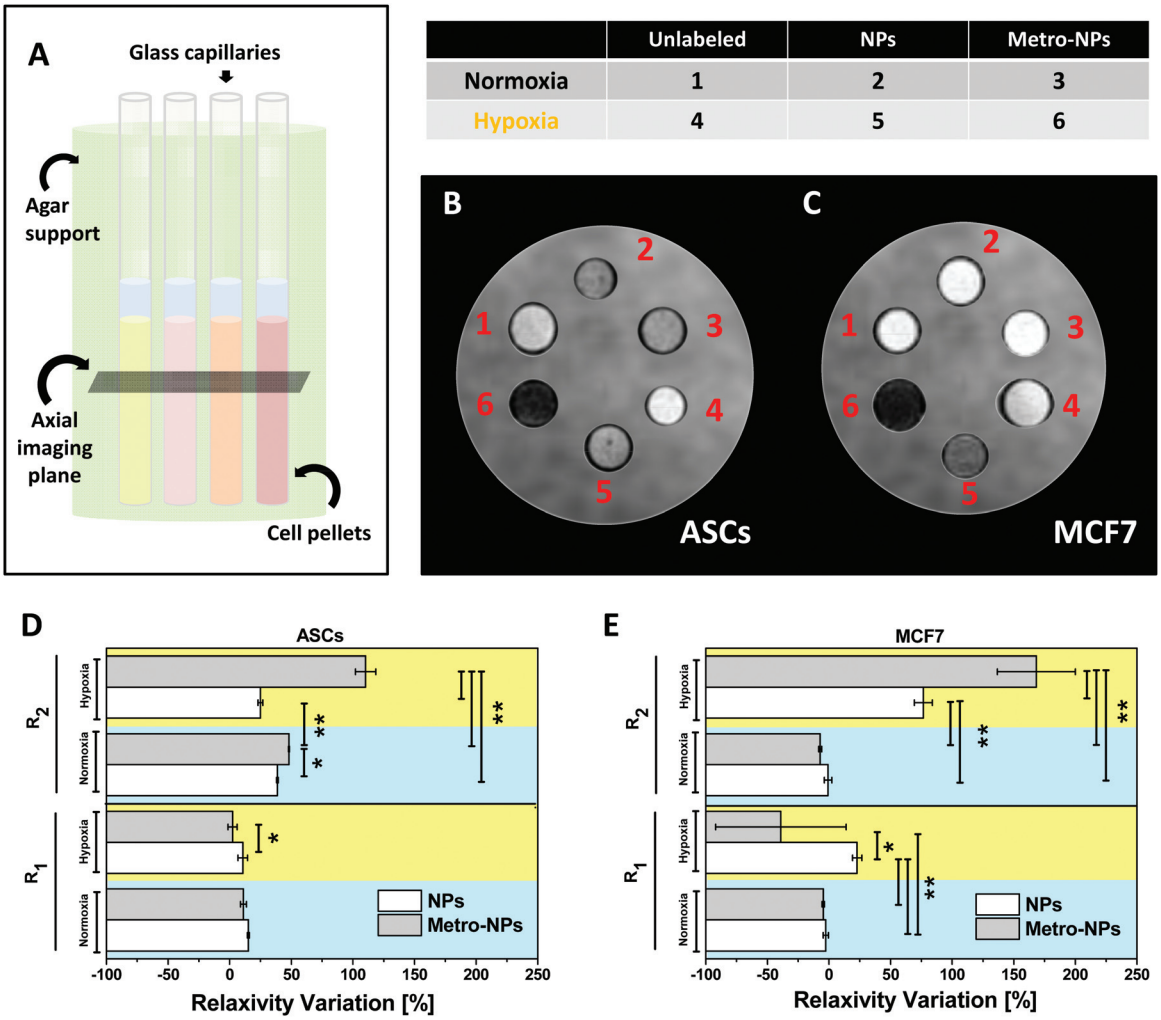

Fig. 7 MRI of hypoxic labeled cells. Representative scheme of the phantom for *in vitro* cellular MRI (A) composed of a support in agarose-based gel and glass capillaries containing cell pellets. Multislice imaging of cell pellets was performed on the axial plane. Representative $T_{2\ w}$-MRI of the pellets of ASCs or MCF7 cells (B and C) 3 days after incubation with PBS (1,4), NPs (2,5), and metro-NPs (3,6), and cultured under normoxic (1,2,3) and hypoxic conditions (4,5,6, orange circles). The percentage R_1 and R_2 variation (R_1/R_2 V) values of labeled pellets with respect to unlabeled cells were calculated from standard saturation recovery and MSME acquisition protocols (D and E).

contrast variation shown by the pictures (Fig. 7D and E). No evident effect was noticed on the modulation of longitudinal relaxivity (R_1) and the corresponding contrast variation (Fig. 7D, E, and S18†). R_2/R_1 ratios for all pellets have also been calculated (Fig. S19†), resulting to be particularly high in hypoxic ASCs and MCF7 cells labeled with metro-NPs (≈128 and 224 respectively), therefore confirming qualitative imaging results and demonstrating intense potential of negative contrast generation.

4. Discussion

Cancer remains one of the most challenging research domains in medicine.[39] In this context, innovative theranostic approaches aim to optimize the biological properties of nanocarriers for early-stage tumor detection and targeted therapy. The malignant progression of solid tumors is associated with increased metabolism and reduced vascular supply, resulting in central areas of prominent hypoxia. The adaptive tissue response to the decreased oxygen tension gives rise to biological alterations becoming molecular targets for therapy and diagnostics.[40]

Well-known cytotoxins and radiosensitizers for hypoxic cells, the nitroimidazoles (specifically 2- and 5-nitro derivatives), have been investigated in many clinical studies.[34] In these compounds, the cytotoxicity under hypoxic conditions has been attributed to the reduction of the nitro group, consequently generating reactive alkylating species, forming hydroxyl compounds under deoxygenated conditions, increasing the oxidative damage of DNA, and suppressing intracellular radioprotectors of sulfhydryl compounds.[41] IONPs have also been included in various complex systems for specific recognition of hypoxic tissues.[39,40,42] Interestingly, Mistry *et al.*

proposed a combinatory use of IONPs and nitrite, where the selective reconversion of nitrite to nitric oxide (NO) in hypoxia and low pH induced IONPs extravasation with important implications for the enhancement of conventional and nano-therapeutic drug delivery.[43] However, even though they have been loaded onto nano-sized systems as hypoxic tumor cytotoxins[44] or as inducers of hypoxia-responsive drug releasers,[45] small molecular bioreductive compounds have never been used to functionalize nano-vehicles and direct their interactions with cells. In the present study, we developed a novel metro-conjugated dendron to functionalize IONPs decorated with coating layers composed of biphosphonated dendrons and we preliminarily assessed their potential use in biomedical applications.

In the absence of appropriate outer layers, bare magnetite particles might trigger relevant cytotoxic consequences when the cells experience concentrations above 100 μg mL^{-1} (ref. 46) and the negative effects are dose-dependent.[47] The need to extend the NP hydrophilicity, optional conjugation, and the biocompatibility fueled the engineering of a great diversity of surface coatings. The size, composition, surface charge, and structure of coatings influence IONP cytotoxicity.[48] Since the concentration threshold of the non-toxicity range is strictly dependent on the shell type,[48] our cytotoxicity study covered a range of NP concentrations between 5 and 150 μg Fe mL^{-1}, similar to previous reports.[15] Although metro-NPs exhibited mild cytotoxic effects upon long-term exposure and high concentrations, their overall impact on cell viability was minimal under all other conditions. In particular, the trypan blue assay and the LDH release tests demonstrated no massive loss of membrane integrity due to the NPs. The lack of effects on the cell activities (such as proliferation or metabolism) confirmed the biological inertness of the nanomaterials on the cell lines of two different origins. Interestingly, no relevant differences in the internalization rate were noticed between endothelial cells and macrophages, even though a more efficient uptake was expected from phagocytic macrophages. By measuring the cellular iron content over time, fast internalization was observed, showing their high cell loading efficiency, consistent with other nanoformulations and labeling procedures,[37,38] which qualifies our NPs as promising tools for sensitive imaging and cell tracking.[38] Moreover, the uptake process at least partially relied on the endocytic pathway, in accordance with the receptor-mediated endocytosis mechanism widely reported in standard labeling procedures based on the direct co-incubation of cells and nanomaterials.[49–51] The good stability shown in buffers and biological media suggests our nanoformulation to be highly suitable for *in vitro* experiments. However, the description of nanosystem interaction with human blood components is also of extreme importance, since most of the future applications of biomedical NPs are based on intravenous/oral administration. Our NPs were stable when exposed to plasma components such as HSA, which, accounting for half of all serum proteins, is the most abundant protein in human plasma (600–700 μM),[52] and also when exposed to complete human reconstituted serum, suggesting good potential for successful intra-systemic injection. Moreover, the assessment of the haemolytic impact is a necessary part of early preclinical research, as hemolysis can lead to jaundice, anemia, and other abnormal conditions.[53] Here, the hemolysis assays did not highlight any specific haemolytic effect due to the metro-functionalization or the nanoplatform itself. The low impact on RBCs might decrease the potential elimination by macrophages through phosphatidylserine- and scavenger receptor-mediated phagocytosis,[53] and hence prolong the NP circulating time. The first part of this work proved that in general terms, despite a slight change in the external surface charge, the metro-NPs and their untargeted counterpart display similar properties and equivalently behave when interacting with normoxic biological systems, such as cell cultures, 3D tissue constructs and biomimetic fluids.

In all cells, the nitroimidazole ligands undergo a variety of enzymatic one-electron decreases, building up a steady-state level of 1 e^- radical anions. This anion reacts preferentially with O_2, thus returning the tracer to its original form. However, in the absence of O_2, it accepts another e^- to produce an intermediate that is sequentially reduced to an efficient nucleophile, the R–NH_2, which can be easily alkylated. Its covalent bonding to macromolecules finally results in cellular retention of the tracer.[22–24] The enzyme xanthine oxidases play a catalytic role in these reactions and may further reduce cellular components.[25] Based on their role as hypoxia-selective cytotoxins for cancer treatment, nitroheterocyclic compounds have started to be loaded onto colloidal carrier systems like solid lipid nanoparticles to enhance tumor drug uptake,[20] and are always more frequently involved in the preparation of various hypoxia-activated and redox-responsive drug delivery nanocarriers.[54–56] In this study, we postulated that in a reducing environment the exposure of metronidazole on the surface could facilitate the interaction and aggregation of NPs with intracellular components, leading to longer retention times. Indeed, we observed that metro-NP deposits remained inside the cells longer in chemically induced-hypoxia or following long-term cell preconditioning to low oxygen tension. Interestingly, even if based on the endocytosis-mediated internalization as expected for several conventional formulations of nanomaterials,[49–51] the intracellular trafficking route of our NPs apparently did not interfere with their capability to accumulate in the cells under hypoxic conditions. Nevertheless, the exact mechanism orchestrating the cell-nanoparticle interplay still needs to be elucidated and will therefore be the subject of future investigations to scrutinize how the compartmentalization and the precise intracellular location of NPs over time affects the metronidazole interaction with the surrounding molecules. As expected, a more intense MRI signal was detected in hypoxic cells treated with metro-NPs with respect to control NPs, unlabeled cells and labeled normoxic cells. In normoxia, the extent of the percentage CV induced by metro-functionalizing the NPs was extremely reduced. This behaviour would therefore allow for actual metro-NP-mediated MRI discrimination of hypoxic tissue

regions only, as under the other conditions the signal differences are less pronounced. Finally, even though *in vivo* experiments reporting on the tracking ability, biodistribution, and fate of metro-NPs are still needed in order to confirm their actual applicability as hypoxic probes in complex living systems, their retention in hypoxic tissues is expected to allow long term-monitoring with limited iron homeostasis imbalance and toxicity. In fact, in our formulation the organic coating and the IONP core were connected through covalent binding, a strong bond able to prevent the coating detachment from the oxide surface, thus stabilizing the inner core and avoiding its fast degradation.

In conclusion, we evaluated the effects on the cell functionality of dendronized metro-functionalized IONPs in endothelial cells, macrophages, and SVF cells, showing encouraging results in terms of biocompatibility both in conventional monolayer cultures and 3D tissue-like constructs. Favorable properties of bio-interaction were described, such as limited cytotoxicity and almost negligible impact on the cell metabolism and growth rate. Moreover, the colloidal stability in biomimetic media suggests that the *in vitro* experimentation as well as injection into the circulatory system of living beings are realistic possibilities for these nano-objects, thus paving the way for future studies dedicated to testing the hypoxia-induced accumulation effect in complex *in vivo* environments. Based on these data, we conclude that metro-NPs are good candidates for the further development of agents recognizing hypoxic tissues with relevant impact related to both tumor investigation and *in vitro* tissue engineering.

Conflicts of interest

There are no conflicts of interest to declare.

Acknowledgements

The "NANOTRANSMED" project is co-funded by the European Regional Development Fund (ERDF) and by the Swiss Confederation and the Swiss cantons of Aargau, Basel-Landschaft and Basel-Stadt, in the framework of the INTERREG V Upper Rhine program ("Transcending borders with every project").

References

1 C. Riviere, S. Roux, O. Tillement, C. Billotey and P. Perriat, Nano-systems for medical applications: Biological detection, drug delivery, diagnostic and therapy, *Ann. Chim. Sci. Mater.*, 2006, **31**, 351.
2 G. R. Rudramurthy and M. K. Swamy, Potential applications of engineered nanoparticles in medicine and biology: an update, *Biol. Inorg. Chem.*, 2018, **23**, 1185.
3 M. G. De Morais, V. G. Martins, D. Steffens, P. Pranke and J. A. da Costa, Biological applications of nanobiotechnology, *J. Nanosci. Nanotechnol.*, 2014, **14**, 1007.
4 S. Aftab, A. Shah, A. Nadhman, S. Kurbanoglu, S. Aysıl Ozkan, D. D. Dionysiou, S. S. Shukla and T. M. Aminabhavi, Nanomedicine: An effective tool in cancer therapy, *Int. J. Pharm.*, 2018, **540**, 132.
5 R. S. Riley, C. H. June, R. Langer and M. J. Mitchell, Delivery technologies for cancer immunotherapy, *Nat. Rev. Drug Discovery*, 2019, **18**, 175.
6 M. R. Singh, Application of metallic nanomaterials in nanomedicine, *Adv. Exp. Med. Biol.*, 2018, **1052**, 83.
7 H. Zhang, X. L. Liu, Y. F. Zhang, F. Gao, G. L. Li, Y. He, M. L. Peng and H. M. Fan, Magnetic nanoparticles based cancer therapy: current status and applications, *Sci. China: Life Sci.*, 2018, **61**, 400.
8 N. V. S. Vallabani and S. Singh, Recent advances and future prospects of iron oxide nanoparticles in biomedicine and diagnostics, *3 Biotech*, 2018, **8**, 279.
9 H. Ittrich, K. Peldschus, N. Raabe, M. Kaul and G. Adam, Superparamagnetic iron oxide nanoparticles in biomedicine: applications and developments in diagnostics and therapy, *RoFo*, 2013, **185**, 1149.
10 S. Sharifi, H. Seyednejad, S. Laurent, F. Atyabi, A. A. Saei and M. Mahmoudi, Superparamagnetic iron oxide nanoparticles for in vivo molecular and cellular imaging, *Contrast Media Mol Imaging*, 2015, **10**, 329.
11 Q. Feng, Y. Liu, J. Huang, K. Chen, J. Huang and K. Xiao, Uptake, distribution, clearance, and toxicity of iron oxide nanoparticles with different sizes and coatings, *Sci. Rep.*, 2018, **8**, 2082.
12 F. Vogtle, G. Richardt and N. Werner, *Dendrimer Chemistry, Concepts, Syntheses, Properties, Applications*, Wiley-VCH, Weinheim, 2009.
13 B. Basly, D. Felder-Flesch, P. Perriat, G. Pourroy and S. Begin-Colin, Properties and suspension stability of dendronized iron oxide nanoparticles for MRI applications, *Contrast Media Mol. Imaging*, 2011, **6**, 132.
14 A. Walter, A. Garofalo, A. Parat, J. Jouhannaud, G. Pourroy, E. Voirin, S. Laurent, P. Bonazza, J. Taleb, C. Billotey, L. Vander Elst, R. N. Muller, S. Begin-Colin and D. Felder-Flesch, Validation of a dendron concept to tune colloidal stability, MRI relaxivity and bioelimination of functional nanoparticles, *J. Mater. Chem. B*, 2015, **3**, 1484.
15 A. Casset, J. Jouhannaud, A. Garofalo, C. Spiegelhalter, D. V. Nguyen, D. Felder-Flesch, G. Pourroy and F. Pons, Macrophage functionality and homeostasis in response to oligoethyleneglycol-coated IONPs: Impact of a dendritic architecture, *Int. J. Pharm.*, 2019, **556**, 287.
16 T. Vangijzegem, D. Stanicki and S. Laurent, Magnetic iron oxide nanoparticles for drug delivery: applications and characteristics, *Expert Opin. Drug Delivery*, 2019, **16**, 69.
17 S. K. Parks, Y. Cormerais and J. Pouysségur, Hypoxia and cellular metabolism in tumour pathophysiology, *J. Physiol.*, 2017, **595**, 2439.

18 T. Genova, L. Munaron, S. Carossa and F. Mussano, Overcoming physical constraints in bone engineering: 'the importance of being vascularized', *J. Biomater. Appl.*, 2016, **30**, 940.
19 K. Splith, R. Bergmann, J. Pietzsch and I. Neundorf, Specific targeting of hypoxic tumor tissue with nitroimidazole-peptide conjugates, *ChemMedChem*, 2012, **7**, 57.
20 E. B. Lages, M. B. de Freitas, I. M. Gonçalves, R. J. Alves, C. D. Vianna-Soares, L. A. Ferreira, M. C. de Oliveira and R. B. de Oliveira, Evaluation of antitumor activity and development of solid lipid nanoparticles of metronidazole analogue, *J. Biomed. Nanotechnol.*, 2013, **9**, 1939.
21 D. I. Edwards, Nitroimidazole drugs–action and resistance mechanisms. I. Mechanisms of action, *J. Antimicrob. Chemother.*, 1993, **31**, 9–20.
22 Q. Zhang, H. Huang and T. Chu, *In vitro* and *in vivo* evaluation of technetium-99m-labeled propylene amine oxime complexes containing nitroimidazole and nitrotriazole groups as hypoxia markers, *J. Labelled Compd. Radiopharm.*, 2016, **59**, 14.
23 K. A. Krohn, J. M. Link and R. P. Mason, Molecular imaging of hypoxia, *J. Nucl. Med.*, 2008, **49**, 129S.
24 R. M. Phillips, Targeting the hypoxic fraction of tumours using hypoxia-activated prodrugs, *Cancer Chemother. Pharmacol.*, 2016, **77**, 441.
25 Q. Zhang, Q. Zhang, Y. Guan, S. Liu, Q. Chen and X. Li, Synthesis and Biological Evaluation of a New Nitroimidazole-99mTc-Complex for Imaging of Hypoxia in Mice Model, *Med. Sci. Monit.*, 2016, **22**, 3778.
26 J. V. Brooks, S. K. Furney and I. M. Orme, Metronidazole therapy in mice infected with tuberculosis, *Antimicrob. Agents Chemother.*, 1999, **43**, 1285.
27 A. Garofalo, A. Parat, C. Bordeianu, C. Ghobril, M. Kueny-Stotz, A. Walter, J. Jouhannaud, S. Begin-Colin and D. Felder-Flesch, Efficient synthesis of small-sized phosphonated dendrons: potential organic coatings of iron oxide nanoparticles, *New J. Chem.*, 2014, **38**, 5226.
28 A. Walter, A. Garofalo, C. Ulhaq, C. Lefèvre, J. Taleb, S. Laurent, L. Vander Elst, R. N. Muller, L. Lartigue, F. Gazeau, C. Billotey, D. Felder- Flesch and S. Begin-Colin, Mastering shape and composition to tailor MRI and hyperthermia properties of dendronized iron oxide nanoparticles, *Chem. Mater.*, 2014, **26**, 5252.
29 C. J. Danpure, Lactate dehydrogenase and cell injury, *Cell Biochem. Funct.*, 1984, **2**, 144.
30 D. Lobner, Comparison of the LDH and MTT assays for quantifying cell death: validity for neuronal apoptosis?, *J. Neurosci. Methods*, 2000, **96**, 147.
31 S. Han, H. M. Sun, K. C. Hwang and S. W. Kim, Adipose-Derived Stromal Vascular Fraction Cells: Update on Clinical Utility and Efficacy, *Crit. Rev. Eukaryotic Gene Expression*, 2015, **25**, 145.
32 S. Güven, A. Mehrkens, F. Saxer, D. J. Schaefer, R. Martinetti, I. Martin and A. Scherberich, Engineering of large osteogenic grafts with rapid engraftment capacity using mesenchymal and endothelial progenitors from human adipose tissue, *Biomaterials*, 2011, **32**, 5801.
33 J. Guerrero, S. Pigeot, J. Müller, D. J. Schaefer, I. Martin and A. Scherberich, Fractionated human adipose tissue as a native biomaterial for the generation of a bone organ by endochondral ossification, *Acta Biomater.*, 2018, **77**, 142.
34 J. P. Piret, D. Mottet, M. Raes and C. Michiels, $CoCl_2$, a chemical inducer of hypoxia-inducible factor-1, and hypoxia reduce apoptotic cell death in hepatoma cell line HepG2, *Ann. N. Y. Acad. Sci.*, 2002, **973**, 443.
35 D. Wu and P. Yotnda, Induction and Testing of Hypoxia in Cell Culture, *J. Visualized Exp.*, 2011, **54**, 2899.
36 E. M. Fennema, L. A. H. Tchang, H. Yuan, C. A. van Blitterswijk, I. Martin, A. Scherberich and J. de Boer, Ectopic bone formation by aggregated mesenchymal stem cells from bone marrow and adipose tissue: A comparative study, *J. Tissue Eng. Regener. Med.*, 2017, **12**, e150–e158.
37 O. M. Girard, R. Ramirez, S. McCarty and R. F. Mattrey, Toward absolute quantification of iron oxide nanoparticles as well as cell internalized fraction using multiparametric MRI, *Contrast Media Mol. Imaging*, 2012, **7**, 411.
38 C. Xu, D. Miranda-Nieves, J. A. Ankrum, M. E. Matthiesen, J. A. Phillips, I. Roes, G. R. Wojtkiewicz, V. Juneja, J. R. Kultima, W. Zhao, P. K. Vemula, C. P. Lin, M. Nahrendorf and J. M. Karp, Tracking Mesenchymal Stem Cells with Iron Oxide Nanoparticle Loaded Poly (lactide-co-glycolide) Microparticles, *Nano Lett.*, 2012, **12**, 4131.
39 V. Sanna, N. Pala and M. Sechi, Targeted therapy using nanotechnology: focus on cancer, *Int. J. Nanomed.*, 2014, **9**, 467.
40 C. Wigerup, S. Påhlman and D. Bexell, Therapeutic targeting of hypoxia and hypoxia-inducible factors in cancer, *Pharmacol. Ther.*, 2016, **164**, 152.
41 H. Nagasawa, Y. Uto, K. L. Kirk and H. Hori, Design of hypoxia-targeting drugs as new cancer chemotherapeutics, *Biol. Pharm. Bull.*, 2006, **29**, 2335.
42 I. Antal, M. Koneracka, M. Kubovcikova, V. Zavisova, I. Khmara, D. Lucanska, L. Jelenska, I. Vidlickova, M. Zatovicova, S. Pastorekova, N. Bugarova, M. Micusik, M. Omastova and P. Kopcansky, d,l-lysine functionalized Fe_3O_4 nanoparticles for detection of cancer cells, *Colloids Surf., B*, 2018, **163**, 236.
43 N. Mistry, A. M. Stokes, J. V. Gambrell and C. C. Quarles, Nitrite induces the extravasation of iron oxide nanoparticles in hypoxic tumor tissue, *NMR Biomed.*, 2014, **27**, 425.
44 B. Li, B. Li, D. He, C. Feng, Z. Luo and M. He, Preparation, characterization, and in vitro pH-sensitivity evaluation of superparamagnetic iron oxide nanoparticle-misonidazole pH-sensitive liposomes, *Curr. Drug Delivery*, 2018, **16**, 254.
45 S. J. Tseng, I. M. Kempson, K. Y. Huang, H. J. Li, Y. C. Fa, Y. C. Ho, Z. X. Liao and P. C. Yang, Targeting Tumor Microenvironment by Bioreduction-Activated Nanoparticles for Light-Triggered Virotherapy, *ACS Nano*, 2018, **12**, 9894.
46 S. M. Hussain, K. L. Hess, J. M. Gearhart, K. T. Geiss and J. J. Schlager, *In vitro* toxicity of nanoparticles

in BRL 3A rat liver cells, *Toxicol. in Vitro*, 2005, **19**, 975.

47 H. L. Karlsson, J. Gustafsson, P. Cronholm and L. Moller, Size-dependent toxicity of metal oxide particles-a comparison between nano- and micrometer size, *Toxicol. Lett.*, 2009, **188**, 112.

48 S. J. Soenen, U. Himmelreich, N. Nuytten and M. De Cuyper, Cytotoxic effects of iron oxide nanoparticles and implications for safety in cell labelling, *Biomaterials*, 2011, **32**, 195.

49 X. Chen, F. Tian, X. Zhang and W. Wang, Internalization pathways of nanoparticles and their interaction with a vesicle, *Soft Matter*, 2013, 7592.

50 M. Mahmoudi, K. Azadmanesh, M. A. Shokrgozar, W. S. Journeay and S. Laurent, Effect of nanoparticles on the cell life cycle, *Chem. Rev.*, 2011, **111**, 3407.

51 S. Mayor, R. G. Parton and J. G. Donaldson, Clathrin-independent pathways of endocytosis, *Cold Spring Harbor Perspect. Biol.*, 2014, **6**, pii: a016758.

52 R. N. Moman and M. Varacallo, *Physiology, Albumin*, SourceStatPearls [Internet], StatPearls Publishing, Treasure Island (FL), 2018.

53 M. A. Dobrovolskaia, J. D. Clogston, B. W. Neun, J. B. Hall, A. K. Patri and S. E. McNeil, Method for Analysis of Nanoparticle Hemolytic Properties In Vitro, *Nano Lett.*, 2008, **8**, 2180.

54 T. Thambi, V. G. Deepagan, H. Y. Yoon, H. S. Han, S. H. Kim, S. Son, D. G. Jo, C. H. Ahn, Y. D. Suh, K. Kim, I. C. Kwon, D. S. Lee and J. H. Park, Hypoxia-responsive polymeric nanoparticles for tumor-targeted drug delivery, *Biomaterials*, 2014, **35**, 1735.

55 R. Sharma and S. Kwon, Evaluation of Cytotoxicity and Hypoxic Effect of Nitroimidazole Embedded Nanoparticles, *J. Nanosci. Nanotechnol.*, 2016, **16**, 4554.

56 Y. Zeng, J. Ma, Y. Zhan, X. Xu, Q. Zeng, J. Liang and X. Chen, Hypoxia-activated prodrugs and redox-responsive nanocarriers, *Int. J. Nanomed.*, 2018, **13**, 6551.